






Spin-orbit coupling in photonic graphene

ZHAOYANG ZHANG,¹ SHUN LIANG,¹ FENG LI,^{1,6}  SHAOHUAN NING,¹ YIMING LI,¹
GUILLAUME MALPUECH,² YANPENG ZHANG,¹  MIN XIAO,^{4,5} AND DMITRY SOLNYSHKOV^{2,3,7} 

¹Key Laboratory for Physical Electronics and Devices of the Ministry of Education & Shaanxi Key Lab of Information Photonic Technique, School of Electronic Science and Engineering, Faculty of Electronic and Information Engineering, Xi'an Jiaotong University, Xi'an 710049, China

²Institut Pascal, PHOTON-N2, Université Clermont Auvergne, CNRS, SIGMA Clermont, F-63000 Clermont-Ferrand, France

³Institut Universitaire de France (IUF), F-75231 Paris, France

⁴Department of Physics, University of Arkansas, Fayetteville, Arkansas 72701, USA

⁵National Laboratory of Solid State Microstructures and School of Physics, Nanjing University, Nanjing 210093, China

⁶e-mail: felix831204@xjtu.edu.cn

⁷e-mail: dmitry.solnyshkov@uca.fr

Received 12 February 2020; revised 30 March 2020; accepted 31 March 2020 (Doc. ID 390386); published 6 May 2020

Spin-orbit coupling of electromagnetic waves is one of the most important effects in topological photonics, but so far it has not been studied in photonic graphene implementations based on paraxial configuration, in particular, in atomic vapor cells. We generate experimentally a honeycomb refractive index pattern in such a cell using electromagnetically induced transparency. We demonstrate that an effective spin-orbit coupling appears as a correction to the paraxial beam equations because of the strong spatial gradients of the permittivity. It leads to the coupling of spin and angular momentum at the Dirac points of the graphene lattice. Our results suggest that the polarization degree of freedom plays an important role in many configurations where it has been previously neglected. © 2020 Optical Society of America under the terms of the OSA Open Access Publishing Agreement

<https://doi.org/10.1364/OPTICA.390386>

1. INTRODUCTION

Topological photonics [1,2] is a rapidly growing field, combining fundamental physics and applied optics. The research in this field has brought us new understanding of the fundamental topological properties of optical systems, which are due to the photonic spin-orbit coupling present in various kinds of inhomogeneous photonic systems [3–5]. Photonic spin-orbit coupling (SOC) is a crucial ingredient for solving long-standing problems like optical isolation at a microscopic scale [6–10] required for the functioning of lasers, opening a new field of topological lasers [11–14].

Photonic graphene is a system of a particular interest. The graphene lattice, studied for more than a half-century [15], was one of the first to demonstrate the striking manifestations of the Dirac physics [16] such as the Klein tunneling [17], with enormous potential for applications, which have already found their way to the market [18]. In photonics, the Dirac points of graphene-like lattices offer extended possibilities for the manipulation of optical angular momentum [19] and for the studies of singular optical beams [20]. Recent works address various problems, such as beam conversion [21], intervalley scattering [22], and valley pseudospin dynamics [23]. Different implementations of photonic graphene include coupled waveguides [24], microwave resonators [25], photorefractive nonlinear crystals [23,26], microcavities [9,27–29], and atomic vapor cells [21], as in the present work. While the main feature of the graphene lattice (the presence of the Dirac cones) is present in all these implementations, other properties can be

different. In particular, the SOC in 2D photonic systems such as microcavities is induced by the splitting between the transverse electric and transverse magnetic (TE-TM) polarized modes [4]. It is known to modify the dispersion at the Dirac point [7,30], leading to trigonal warping, like in bilayer graphene [31]. In coupled waveguide arrays, usually only a single polarization mode is used, and the other polarization can be neglected. In nonlinear crystals and atomic vapor cells, the effects of the SOC on the photonic graphene have not been studied so far.

The evolution of a photonic beam in a spatially varying medium is a particularly important fundamental and applied problem. It is often described in the paraxial approximation of the Helmholtz equation [32], especially in the field of nonlinear optics, where it allows us to determine the spatial mode profiles. The coupling of polarizations can arise either due to the anisotropy of the material or to its inhomogeneity [33]. The former usually couples circular polarizations [34] and was already shown to lead to angular momentum transfer [35,36], while the latter has not been fully studied so far. In many cases, the intrinsic coupling of polarizations is simply neglected in the paraxial approximation [33]. Taking it into account in the calculations of the beam trajectory and properties often leads to spectacular effects, such as the spin Hall effect of light [3,37,38].

The behavior of the polarization of light has been described in the limit of geometric optics in the works of Rytov [39]. The Rytov matrix allows the prediction of the rotation of the linear

polarization. For rays belonging to the class of planar curves (that is, lying in a plane), such rotation is absent: the TE field keeps its polarization in the plane. However, if the ray trajectory becomes three-dimensional (3D, e.g., helix trajectory), the linear polarization starts to rotate. This effect gives an important contribution to the depolarization of light beams in turbulent atmosphere [40,41]. The rotation of the polarization was linked with anholonomic effects a long time ago [42] and was shown to lead to the accumulation of the Berry phase [43] shortly after its discovery [44]. However, the corresponding theory was limited to ray tracing, equivalent to considering a point-like particle (beam center of mass) instead of a wave packet (beam envelope), whereas modern research subjects, such as the photonic graphene, clearly require a complete wave theory for the transverse beam evolution. The first attempts to develop such theory have shown that the so-called “form birefringence” arising for a purely isotropic material as a consequence of its spatial inhomogeneities can be described using two different effective potentials for the TE and TM modes [45–47] with second-order corrections (in the refractive index gradient). It was also shown that first-order corrections can appear in twisted anisotropic materials [48].

In this work, we introduce the first-order SOC terms into the paraxial equations for the two transverse polarizations. We experimentally study photonic graphene in a configuration established by coherently prepared multilevel atomic systems, where this SOC plays a dominant role in the observations. We show that SOC couples the spin and angular momentum at the Dirac points, modifying the angular momentum of the probe beam depending on its polarization.

2. MODEL

The Helmholtz equation for the electric field of an electromagnetic wave in a dielectric medium reads

$$\nabla^2 \mathbf{E} + k_0^2 n^2 \mathbf{E} = 0. \quad (1)$$

In a *homogeneous* system, this equation does not contain any SOC terms, and the polarizations are decoupled. This allows writing a paraxial equation for a scalar amplitude, corresponding to a single chosen polarization of light (which is conserved). It is very well known that this paraxial equation is equivalent to the time-dependent Schrödinger equation for a wave function of a scalar particle.

However, when the spatial gradients are not negligibly small and when the polarization effects are explicitly studied, the SOC has to be taken into account. It is associated with a coupling of the two polarizations, TE and TM [45], which become well-defined in the presence of any gradient (to which they are transverse, in addition to being perpendicular to the propagation direction). Equation (1) in this case gives rise to *two* paraxial equations for two field projections, which are in general coupled. This coupling can be considered as a correction to uncoupled equations. It is usually second order in the gradient, but first-order terms can also appear. In geometric optics, the SOC leads to the evolution of the transverse linear polarization along a curved beam [39]. This adiabatic evolution has been shown to lead to dramatic effects, such as the spin Hall effect of light [3,37,49], considered also in vapor cells [50]. Coming back to the analogy with quantum mechanics, the geometric optics corresponds to studying a classical particle, whereas the paraxial equation corresponds to considering

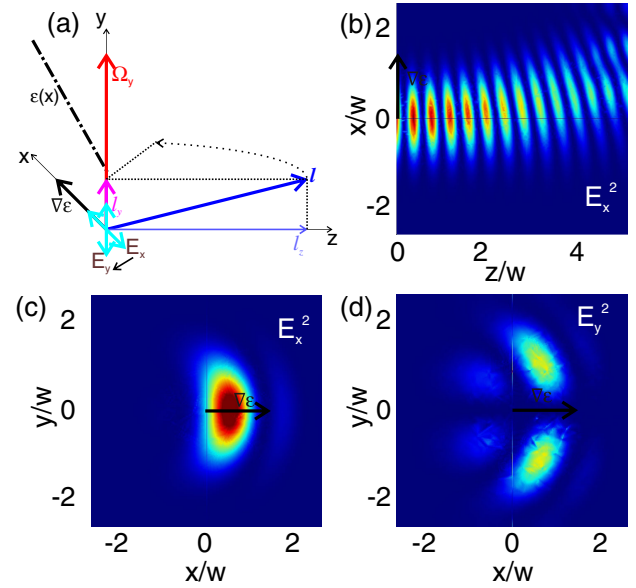


Fig. 1. Polarization conversion under a constant gradient $\nabla\epsilon$ (black arrow). (a) Scheme of the effect: \mathbf{k} is the wave vector of light (direction \mathbf{l} , blue arrow), Ω is the rotation frequency (red arrow) due to the permittivity gradient $\nabla\epsilon$, with the permittivity profile $\epsilon(x)$ shown as a black dashed–dotted line; (b) beam trajectory in the XZ plane (curved due to the gradient $\nabla\epsilon$). Transverse beam profiles: (c) in the XY plane in the E_x polarization. Shift along x is due to $\nabla\epsilon$; (d) in the XY plane in the E_y polarization entirely generated due to SOC, proportional to $\Omega \cdot \mathbf{k} \sim k_y$ (zero at $y = 0$).

an equivalent quantum wave packet. Starting from the evolution of the polarization in the spin Hall effect of light for a beam in the geometric optics limit, that is, for a classical propagating particle, we show how this term is introduced into paraxial equations for the two projections of the electric field amplitude, leading to an original type of SOC. This is especially important for the study of the propagation of beams in such systems as photonic graphene, whose energy bands appear from the quantum mechanical description.

As pointed out already by Rytov [39], the linear polarization can rotate only for a nonplanar beam trajectory. Noting the beam direction as $\mathbf{l} = \mathbf{k}/k$ and the vector of its rotation as Ω , the relevant quantity describing the part of its rotation that is not in a plane can be written as $\Omega \cdot \mathbf{l}$. This is illustrated by a scheme in Fig. 1(a). It was shown that the rotation of the transverse polarization adds an extra term to the Helmholtz equation for the TE field,

$$\nabla^2 \mathbf{E}_\perp + k_0^2 n^2 \mathbf{E}_\perp + 2ink_0 (\Omega \cdot \mathbf{l}) [\mathbf{l} \times \mathbf{E}_\perp] = 0. \quad (2)$$

This term introduced in Ref. [44] can be understood as an analog of the Coriolis force, appearing in a noninertial frame, whose noninertial nature is due precisely to the rotation Ω . The geometric optics limit of this equation has allowed to describe the spin Hall effect of light [49].

In order to include this term into the paraxial equations, we need to link Ω with the transverse field \mathbf{E} and the dielectric permittivity ϵ or the dielectric susceptibility χ . Let us consider a beam with its main propagation direction along z , containing nonzero x and y wave vector harmonics because of its transverse profile, in presence of a gradient along x , $\partial\epsilon/\partial x \neq 0$ (black arrows in Fig. 1), which leads to the deviation of the beam from its initial direction, $\Omega_y = (2n)^{-1} \partial\epsilon/\partial x$. The projection of the rotation frequency on the direction of a particular harmonic is given by

$$\Omega \cdot \mathbf{I} = \frac{k_y}{2nk_0} \frac{\partial \epsilon}{\partial x}. \quad (3)$$

In order to illustrate that the polarization conversion indeed takes place in such conditions, we perform a finite-difference time domain (FDTD) numerical simulation of the propagation of a Gaussian beam using COMSOL in the simplest system described above. The results are shown in Figs. 1(b)–1(d). The trajectory of the beam, curved by the gradient $\partial \epsilon / \partial x$, is shown in Fig. 1(b). The beam is initially excited with E_x polarization only. The transverse profile in this polarization is shown in Fig. 1(c). The beam is shifted towards positive x , as in Fig. 1(b). Its shape also changes. But the most important effect is shown by Fig. 1(d), presenting the cross-polarization E_y , appearing only because of the SOC. This requires a nonzero projection of the wave vector \mathbf{k} on its rotation frequency Ω , according to Eq. (3), which is fulfilled thanks to the presence of nonzero k_y in the narrow initial Gaussian beam. The intensity of converted polarization is linear in $\nabla \epsilon$, confirming the first-order nature of the effect. We note that since the converted signal is proportional to k_y , it changes sign at $y = 0$: the symmetry of the state is inverted (from symmetric to antisymmetric). This will be important for the understanding of SOC effects in a periodically modulated medium (lattice). In spite of being linear in $\nabla \epsilon$, the SOC represents only a small correction in the conditions of Fig. 1: the converted polarization intensity remains small for realistic gradients, and its detection requires a fine tuning of the polarizer to avoid being blinded by the main polarization. Below, we will see how the contribution of SOC can become dominant in a more complicated configuration.

Our goal is to obtain paraxial equations valid for an arbitrary permittivity profile and written in a fixed polarization basis (and not TE and TM, which differ from point to point). We have therefore to generalize the previous result to arbitrary gradient directions. The wave vector \mathbf{k} also has to be expressed from $\mathbf{E}(x, y)$ using $k_{(x,y)} = -i\partial/\partial(x, y)$. One obtains the following SOC term:

$$\frac{1}{2nk_0|E_{\perp}|} \left(\frac{\partial \epsilon}{\partial x} \frac{\partial E_x}{\partial y} + \frac{\partial \epsilon}{\partial y} \frac{\partial E_y}{\partial x} \right) \mathbf{I} \times \mathbf{E}_{\perp}. \quad (4)$$

As compared with TE-TM SOC in planar cavities [4,51] and photonic crystal slabs, the double spatial derivative of the electric field is replaced by a product of the first derivatives of the permittivity and the electric field components.

The paraxial approximation consists in considering the envelope of the electric field and neglecting $\partial^2 \mathbf{E}_{\perp} / \partial z^2$ with respect to $k_0 \partial \mathbf{E}_{\perp} / \partial z$ in the first term of Eq. (1) (z is the main propagation direction). In atomic systems, the permittivity can be varied through the effect of electromagnetically induced transparency (EIT) [52]. Another polarization effect that obviously needs to be taken into account in the presence of EIT under polarized pumping is the polarization-dependent complex permittivity. This is naturally included in the paraxial equations via $\epsilon_{x,y}$ or susceptibility $\chi_{x,y}$ with real and imaginary parts (marked by ' and ', correspondingly, the latter being much smaller than the former). The imaginary part of susceptibility is taken into account in the effective potential term $k_0 \chi_i E_i / 2$ for each polarization, but neglected in the SOC terms, where it would represent a next-order correction. The SOC terms therefore contain only the real part of the susceptibility, $\partial \epsilon / \partial(x, y) \sim \partial \chi' / \partial(x, y)$. The vector product $\mathbf{I} \times \mathbf{E}_{\perp}$ of Eq. (2), Eq. (4) gives rise to the coupling of the two polarizations $E_{(x,y)}$. The final paraxial equations taking into

account the SOC and the polarization-dependent propagation in the linear polarization basis read

$$i \frac{\partial E_x}{\partial z} = -\frac{1}{2k_0} \left(\frac{\partial^2}{\partial x^2} + \frac{\partial^2}{\partial y^2} \right) E_x - \frac{k_0 \chi_x}{2} E_x + \frac{1}{2k_0 |E|} \left(\frac{\partial \chi'_x}{\partial x} \frac{\partial E_x}{\partial y} + \frac{\partial \chi'_y}{\partial y} \frac{\partial E_y}{\partial x} \right) E_y, \quad (5)$$

$$i \frac{\partial E_y}{\partial z} = -\frac{1}{2k_0} \left(\frac{\partial^2}{\partial x^2} + \frac{\partial^2}{\partial y^2} \right) E_y - \frac{k_0 \chi_y}{2} E_y + \frac{1}{2k_0 |E|} \left(\frac{\partial \chi'_x}{\partial x} \frac{\partial E_x}{\partial y} + \frac{\partial \chi'_y}{\partial y} \frac{\partial E_y}{\partial x} \right) E_x. \quad (6)$$

Of course, the importance of the corrective SOC term depends on the conditions of a given experiment. We will compare the predictions of these paraxial equations with the solution of the full system of Maxwell's equations and with the experimental measurements for a particular system of photonic graphene and show that, when the imaginary susceptibilities are different, the contribution of the SOC into the signal observed for a faster-decaying polarization component actually becomes dominant.

3. EXPERIMENTAL IMPLEMENTATION OF PHOTONIC GRAPHENE

While the SOC plays a significant role in a large variety of optical systems, we investigate its effect in a particularly interesting process: the vortex generation at the Dirac points in photonic graphene. Our experiments are performed in atomic vapors in the regime of EIT. Figure 2 shows the scheme of the experiment for exciting a given valley in the photonic graphene lattice. Three Gaussian coupling beams E_2 , E'_2 , and E''_2 (wavelength $\lambda_2 \approx 794.97$ nm; frequency ω_2 ; vertical polarization; Rabi frequencies Ω_2 , Ω'_2 , and Ω''_2 , respectively) from the same external cavity diode laser (EDCL2) symmetrically propagate along the z direction and intersect at the center of the vapor cell with the same angle of $2\theta \approx 1.2^\circ$ between any two of them to form a hexagonal optical lattice [see Fig. 2(d)], acting as the coupling field with an intensity of $|\Omega_c|^2$. The Rabi frequency of a transition $|i\rangle \leftrightarrow |j\rangle$, defined by $\Omega_l = \mu_{ij} E_l / \hbar$, where E_l is the electric field from the laser and μ_{ij} is the dipole momentum (i, j , and l are integer numbers), is quantitative characterization of the coupling between the optical field and its corresponding two-level atomic system. The hexagonal lattice appears as a result of interference, and thus does not suffer from any broadening due to diffraction. The 5 cm long atomic vapor cell wrapped with μ -metal sheets is heated to 80° by a heat tape. The copropagating probe field and coupling field interact with a Λ -type three-level ^{85}Rb atomic system [see Fig. 2(b)], which consists of two hyperfine states $F = 2$ (level $|1\rangle$) and $F = 3$ ($|2\rangle$) of the ground state $5S_{1/2}$, and an excited state $5P_{1/2}$ ($|3\rangle$). Here, the probe field [Fig. 2(c)] is established by the interference of two probe beams E_1 and E'_1 ($\lambda_1 \approx 794.98$ nm, ω_1 , Ω_1 , and Ω'_1 , respectively) derived from the same ECDL1. The powers of the three Gaussian coupling beams are all 15 mW, and of the two Gaussian probe beams are both ~ 0.5 mW. All the coupling and probe beams have the same diameter of ~ 1 mm. The polarizations of the beams are indicated as X (horizontal), Y (vertical), and $X + iY$ (circular). A polarization beam splitter (PBS) is mounted in front of the charge-coupled device (CCD) camera to filter out the coupling beam,

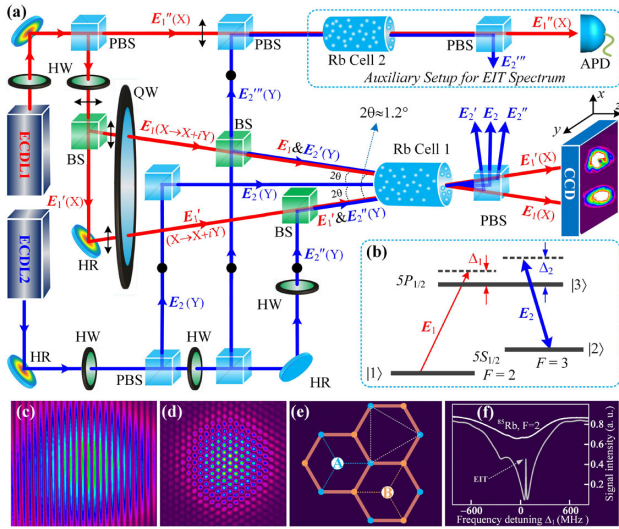


Fig. 2. Illustration of the experimental setup and principles. (a) Experimental setup. ECDL, external cavity diode laser; HW, half-wave plate; QW, quarter-wave plate; HR, high-reflection mirror; PBS, polarization beam splitter; BS, beam splitter; APD, avalanche photodiode detector; CCD, charge-coupled device camera. The beam intensities are controlled by corresponding tunable attenuators. Double-headed arrows and filled dots denote horizontal polarization (X) and vertical polarization (Y) of the beams, respectively. Circular polarization is obtained as $X + iY$. (b) The three-level Λ -type ^{85}Rb atomic energy-level structure. Term Δ_1 (Δ_2) is the frequency detuning between the atomic resonance $|1\rangle \rightarrow |3\rangle$ ($|2\rangle \rightarrow |3\rangle$) and the probe (coupling) frequency. (c) The standing-wave probe field formed by E_1 and E_1' . (d) The formed hexagonal optical lattice by E_2 , E_2' , and E_2'' . (e) The schematic diagram for the A- and B-type sublattices on a graphene structure. (f) The observed absorption (upper curve) and EIT (lower curve) spectra from the auxiliary setup [marked by the dashed box in the upper right corner of (a)]. The EIT spectrum is generated by injecting beams E_1' and E_2'' (from the same laser as E_1 and E_2 , respectively) into the Rb cell 2 and received by an APD.

which is set as y polarized throughout the experiment, allowing only the detection of the x polarized component of the probe beam [see Fig. 2(a)].

With the two-photon resonant condition $\Delta_1 - \Delta_2 = 0$ satisfied (here $\Delta_1 \sim 70$ MHz), an EIT window [52] can occur on the transmitted probe spectrum of the probe field. For an EIT configuration, the susceptibility $\chi = \chi' + i\chi''$ experienced by the probe field is $\chi \sim |\Omega_c|^{-2}$ [53], and the resulting susceptibility (both real part χ' and imaginary part χ'') exhibits a honeycomb profile with a lattice constant $a \approx 25$ μm , which corresponds to an inverted hexagonal $|\Omega_c|^2$ [21]. For a three-level EIT atomic system, the real and imaginary parts of the refractive index are described by $n_R = \chi'/2$ and $n_I = \chi''/2$, respectively [54,55]. As a result, a photonic graphene lattice governed by $n_R(x, y)$ is effectively “written” inside the medium. The refractive index variation and absorption spectrum are polarization-dependent. As presented in Fig. 3 of Ref. [56], for the copolarized configuration of the coupling and probing beams, the absorption of the probe beam around zero detuning is greatly reduced by the depletion of the ground state with optical pumping, while hardly any EIT effect occurs. For the cross-polarized configuration, there is clearly the EIT effect around zero detuning, while the absorption of the probe beam is also relatively strong. As a result, around zero detuning, χ' and χ'' are approximately 5 and 20 times smaller for the copolarized component (depleted, y) than for the cross-polarized one

(EIT, x). The characteristic scales are $\chi'_x \sim 10^{-3}$, $\chi''_x \sim 10^{-4}$ and $\chi'_y \sim 2 \times 10^{-4}$, $\chi''_y \sim 5 \times 10^{-6}$ (for a y -polarized pump, i.e., the coupling beam).

The A- and B-type sublattices of the optically induced two-dimensional (2D) photonic graphene are marked in Fig. 2(e). By selectively covering only the A or the B sublattice with the periodic probe field as in Fig. 2(c), the K or K' valley in the momentum space can be effectively excited, which, due to the beam conversion between the sublattices, introduces an orbital angular momentum (OAM) to one of the output probe beams [21,23], confirmed by a fork-like feature in the interference pattern with a Gaussian reference beam (from the same laser as probe beams). Indeed, when the probe is exciting only A -sites of the graphene lattice, its conversion to the B -sites is accompanied by the change of angular momentum according to $l_B = l_A - 1$. This interesting feature of the Dirac equation shown by previous studies [21,23] can be understood or described using different approaches or languages used in different fields of physics. Mathematically, it arises from the fact that the coupling between the two components of the spinor written in the reciprocal space depends on the azimuthal angle: $\hat{H} = \hbar c \mathbf{k} \cdot \boldsymbol{\sigma}$ (where $\boldsymbol{\sigma}$ is a vector of Pauli matrices). The equation for the generated component reads $i\hbar \dot{\psi}_B = \hbar c k e^{i\phi} \psi_A$. Because of the coefficient $e^{i\phi}$, the angular momentum operator $i\partial/\partial\phi$ applied to ψ_B gives $l_B = l_A - 1$. The change of the angular momentum can also be interpreted as a result of the nonzero Berry curvature of the graphene bands in the vicinity of the Dirac point [57]. Using the pseudospin language, it can be understood as a result of the action of a divergent effective field [58,59].

Both the transmitted probe beam and phase (interference pattern) are monitored by a CCD. To investigate the influence of the polarization of the probe beams on the OAM creation from the valley pseudospin, a quarter-wave plate is applied on the path of the probe beams before entering the atomic vapor cell, allowing varying of the probe polarization. It should be noted that regardless of the probe beam polarization, the CCD always detects a single linear polarization component (x) defined by the PBS before it. The detected image contains signal from both graphene sublattices, but changing the detuning allows us to select a particular moment of “time” (half of the $A \leftrightarrow B$ conversion period), when all intensity is coming from the nonexcited sublattice B , allowing the observation of the modified angular momentum l_B .

4. RESULTS AND DISCUSSION

We are now considering polarized light described by a two component wave function propagating in the photonic graphene lattice. In general, solving 2D paraxial equations is much more efficient than solving the full system of Maxwell’s equations in 3D. We begin our analysis with the comparison of the results of the two different numerical approaches for the simple case of a Gaussian probe of a width w exciting the vicinity of the Dirac point of graphene, and neglecting the photonic SOC. In such a case, the evolution of the beam is well described by the 2D Dirac equation describing the coupling between A and B sites of the honeycomb lattice. This approximation remains valid even including SOC when both excitation and detection are carried out in the same linear polarization (in this case, the contribution of SOC is negligible). The conversion between the two sites associated with the change of the angular momentum can be obtained both with the 3D finite-element method (FEM) and 2D paraxial equations, as shown in Figs. 3(a)

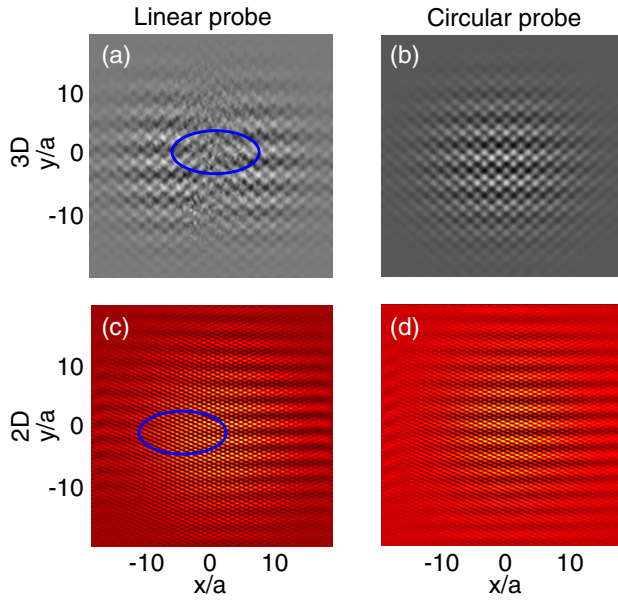


Fig. 3. Theoretical simulation of interference patterns between the reference and probe beams after photonic graphene: (a), (b) 3D and (c), (d) 2D models: (a), (c) linear and (b), (d) circular probe. The dislocations indicating optical vortices are present only for linear probe.

and 3(c), and, naturally, with the Dirac equation (which is an extra approximation with respect to the paraxial equation), as discussed above. The interference patterns in panels Figs. 3(a) and 3(c) show the fork-like dislocation, which is a signature of a nonzero final angular momentum, $l_B = -1$ (initially, $l_A = 0$). We note that the $A \rightarrow B$ conversion period $T = w/c$ depends on χ via the effective speed of light in the Dirac equation c .

The situation changes when the excitation contains both E_x and E_y (circular pumping), and the SOC starts to play a role. Figures 3(b) and 3(d) show interference patterns between the transmitted amplitude in the x polarization and a reference beam. It does not show any dislocations in the fringe patterns. The absence of angular momentum conversion is a joint result of three different effects. First, the y -polarized component exhibits a slower $A \rightarrow B$ conversion because of a smaller real susceptibility $\chi'_y \approx 0.2\chi'_x$. So, E_y does not change angular momentum during the propagation time in the cell. The second effect is the smaller decay of the y component, because of a smaller imaginary susceptibility $\chi''_y \approx 0.05\chi''_x$. As a result, the E_y component quite rapidly becomes dominant over E_x , and most of the x -polarized light is induced by the E_y to E_x conversion by the SOC. Ultimately, the E_x generated by the SOC is not affected by the angular momentum conversion because the corresponding wave function is not anymore close to the Dirac point but lies in an upper band of graphene as explained below. As a result of these combined processes, the angular momentum $L = 0$ measured in E_x in Figs. 3(b) and 3(d) is that of l_A injected in E_y , and we can conclude that the angular momentum of the light after the cell is controlled by the incoming polarization.

Let us first make a simple estimate proving that the contribution of the polarization conversion can indeed become dominant with respect to the rapidly decaying original signal. The relevant terms in the paraxial equation for the description of the intensity contributions to the detected polarization E_x become

$$i \frac{\partial E_x}{\partial z} = -\frac{ik_0\chi''_x}{2}E_x + \frac{1}{2k_0|E|} \frac{\partial \chi'_y}{\partial y} \frac{\partial E_y}{\partial x} E_y. \quad (7)$$

The first term provides an exponential decay with a characteristic rate $k_0\chi''_x \approx 10^7 \times 10^{-4} = 10^3 \text{ m}^{-1}$, while the second one provides a linear growth (assuming $E_y = \text{const}$ as compared with E_x). To estimate its rate, we use the experimental parameters $k_x/k_0 \approx \theta \approx 10^{-2}$ and $\partial \chi'_y/\partial x \approx 10^{-4}/25 \times (10^{-6}) = 4$, which gives a rate of the order of 10^{-2} . Comparing an exponential decay $\exp(-10^3 z)$ with a linear growth $10^{-2} z$ for identical initial intensity (circular pumping), we see that the two contributions become equal within a propagation distance of 1 cm. We can therefore conclude that for a 5 cm vapor cell the contribution of the SOC-induced polarization conversion can indeed be important and even dominant. A more detailed discussion of the evolution of the intensities based on rate equations is given in Supplement 1. With these estimates, the advantage of using photonic graphene becomes clear. Indeed, in the constant gradient configuration of Fig. 1 for the same parameters but without the decay caused by χ'' , the intensity of converted polarization given by the conversion rate 10^{-2} m^{-1} times the propagation distance $5 \times 10^{-2} \text{ m}$ would be only 5×10^{-4} of the main polarization, which would represent a correction impossible to detect. This is why it is important to use the photonic graphene, where we have a clear qualitative signature of the efficiency of the polarization conversion: the presence or the absence of a vortex. We also note that all the terms in the paraxial equations remain small with respect to the main wave vector k_0 , which ensures the validity of the approximation itself.

The other crucial effect is the absence of angular momentum conversion for the E_x polarization induced by SOC. This can be understood by using arguments based on tight-binding description (while the development of a complete tight-binding model accounting for the specific SOC is beyond the scope of the present work). The SOC terms contain the first-order derivatives of the wave function. It thus inverts the mode symmetry, coupling the s (symmetric) and p (antisymmetric) orbitals of each minimum of the effective lattice potential. Indeed, in Fig. 1, a single maximum (Gaussian, s -orbital) was converted into an antisymmetric double-maximum structure (p -orbital). The converted polarization therefore appears at the same valley, but in the p band. The shape of the wave function suggests that conversion occurs toward the flat p band of the honeycomb potential [27], where further evolution is completely blocked (see Supplement 1 for more details). This is why the converted component maintains its original angular momentum. The observed signal is the superposition of the original component E_x (changing the angular momentum) and the signal converted from E_y (keeping the original angular momentum). The final result depends on the relative intensities of the two components, and varying their initial ratio (which is the circular polarization degree) allows us to observe the vortex leaving the beam center step by step, when the circular polarization is increased (see below for the experimental results), similar to the spatial dynamics observed in Ref. [21], but in the opposite direction.

The comparison of the 3D and 2D results demonstrates the correctness of the developed corrected paraxial equations. In what follows, we are going to use only the 2D model and to consider a probe with nonzero initial angular momentum. Figure 4 shows the results of numerical simulations with 2D coupled paraxial equations for the case of the Gauss-Laguerre probe envelope with $L = -1$ [Figs. 4(a) and 4(b)] and $L = +1$ [Figs. 4(c) and 4(d)] with linear [Figs. 4(a) and 4(c)] and circular [Figs. 4(b) and 4(d)]

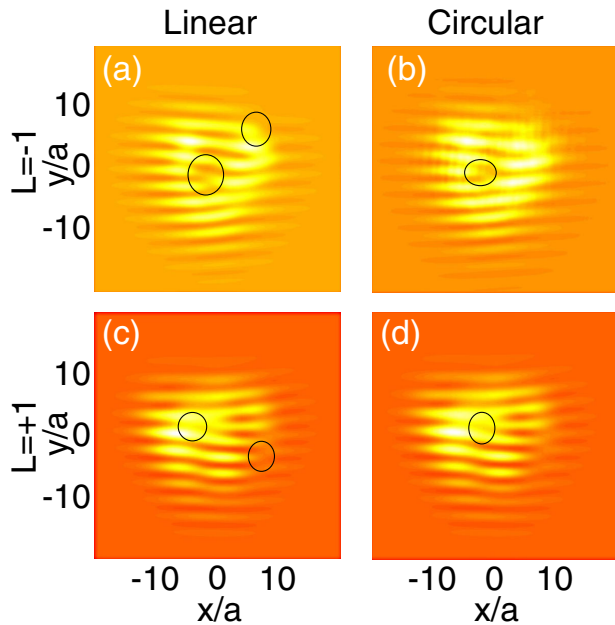


Fig. 4. Theoretical simulations of the interference patterns of separated single-valley beams with a reference beam (2D paraxial equation). Different initial angular momentum: (a), (b) $L = -1$ and (c), (d) $L = +1$; different initial polarization: (a), (c) circular and (b), (d) linear.

probe polarization. For $L = -1$ and linear excitation, the beam conversion introduces an extra vortex into the pattern, giving $L_{\text{out}} = -2$. For $L = +1$, the sign of the extra vortex is opposite to the initial angular momentum, and $L_{\text{out}} = 0$. This extra vortex disappears in both cases if the initial polarization is circular, because the output beam is dominated by the E_y converted to E_x . A crucial advantage of using a 2D model here is that it allows a more extended treatment of the output field distributions, in particular, valley separation and interference analysis (based on Fourier transform and shifting in the reciprocal space), similar to the beam separation after the vapor cell in the experiment [21].

Finally, in Fig. 5, we present the results of the experimental measurements carried out in the configuration described in the previous section, for three values of the angular momentum of the inbound Gauss–Laguerre probe: (a) $L = 0$ (as in Fig. 3), (b) $L = -1$, and (c) $L = +1$ (as in Fig. 4). The false color scale represents the intensity of the interference pattern, measured at the screen after the vapor cell in the x polarization. The interference occurs between one of the two probe beams and a reference beam. The numbered panels represent the increase of the circular polarization degree from $\rho_c = 0$ [Fig. 5(a1, b1, c1)] to $\rho_c = 1$ [Fig. 5(a5, b5, c5)]. The experimental observations correspond to the theoretical images shown above: in each case, the extra vortex brought into the beam by the interaction with graphene lattice disappears when ρ_c is increased, because signal is dominated by the converted component. We note that while the exact values of the susceptibility of the atomic vapors are not known with a high precision, our qualitative results are robust with respect to these parameters; additional simulation results for a set of parameters different from those of the main text are given in Supplement 1.

In all three cases, we observe that the SOC allows controlling the angular momentum of the output beam via both the polarization and momentum of the input beam. Devices with

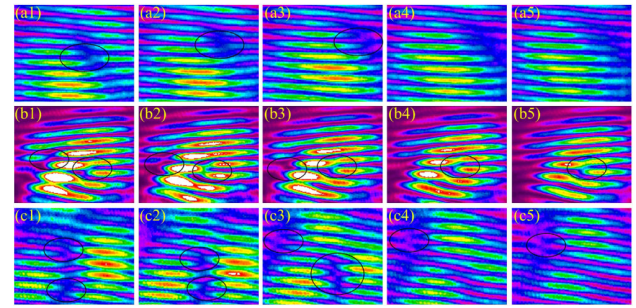


Fig. 5. Experimental interference images for different GL beams: (a) $L = 0$; (b) $L = -1$; (c) $L = +1$. Numbers correspond to circular polarization degree: from $\rho_c = 0$ [linear probe (a/b/c1)] to $\rho_c = 1$ [circular probe (a/b/c5)]. In each case, the change of polarization induces the decrease of the output beam angular momentum by 1.

an optically controllable optical angular momentum are useful for practical applications, but creating them is a challenging task [60]. Our experiment provides a solution of this problem, while demonstrating the fundamental importance of SOC in the paraxial approximation, which has been neglected so far. In future works, we will develop the tight-binding description of this original type of SOC. It is also interesting to study how this particular SOC affects the nonlinear solutions of the paraxial equations, such as bright solitons. Nontrivial polarization textures can be expected to appear in this case.

To conclude, we introduced a first-order correction to paraxial equations due to the SOC linked with the conservation of the polarization plane. We demonstrated experimental evidence of the importance of this SOC in photonic graphene implemented via EIT in atomic vapors. The angular momentum of the output beam can be controlled by the circular polarization of the probe.

Funding. National Key Research and Development Program of China (2018YFA0307500, 2017YFA0303703); National Natural Science Foundation of China (11804267, 61975159); Fundamental Research Funds for the Central Universities (xjj2017059); Agence Nationale de la Recherche (16-IDEX-0001, ANR-11-LABX-0014, ANR-16-CE30-0021).

Acknowledgment. We acknowledge the support of the project “Quantum Fluids of Light,” of the ANR Labex Ganex, and of the ANR program “Investissements d’Avenir” through the IDEX-ISITE initiative 16-IDEX-0001 (CAP 20-25).

Disclosures. The authors declare no conflicts of interest.

See Supplement 1 for supporting content.

REFERENCES

1. L. Lu, J. D. Joannopoulos, and M. Soljačić, “Topological photonics,” *Nat. Photonics* **8**, 821–829 (2014).
2. T. Ozawa, H. M. Price, A. Amo, N. Goldman, M. Hafezi, L. Lu, M. C. Rechtsman, D. Schuster, J. Simon, O. Zilberberg, and I. Carusotto, “Topological photonics,” *Rev. Mod. Phys.* **91**, 015006 (2019).
3. M. Onoda, S. Murakami, and N. Nagaosa, “Hall effect of light,” *Phys. Rev. Lett.* **93**, 083901 (2004).
4. A. Kavokin, G. Malpuech, and M. Glazov, “Optical spin Hall effect,” *Phys. Rev. Lett.* **95**, 136601 (2005).

5. K. Y. Bliokh, D. Smirnova, and F. Nori, "Quantum spin Hall effect of light," *Science* **348**, 1448–1451 (2015).
6. Z. Wang, Y. Chong, J. D. Joannopoulos, and M. Soljačić, "Observation of unidirectional backscattering-immune topological electromagnetic states," *Nature* **461**, 772–775 (2009).
7. A. V. Nalitov, D. D. Solnyshkov, and G. Malpuech, "Polariton topological insulator," *Phys. Rev. Lett.* **114**, 116401 (2015).
8. D. Solnyshkov, O. Bleu, and G. Malpuech, "Topological optical isolator based on polariton graphene," *Appl. Phys. Lett.* **112**, 031106 (2018).
9. S. Klembt, T. Harder, O. Egorov, K. Winkler, R. Ge, M. Bandres, M. Emmerling, L. Worschech, T. Liew, M. Segev, C. Schneider, and S. Hofling, "Exciton-polariton topological insulator," *Nature* **562**, 552–556 (2018).
10. D. Karki, R. El-Ganainy, and M. Levy, "Toward high-performing topological edge-state optical isolators," *Phys. Rev. Appl.* **11**, 034045 (2019).
11. D. D. Solnyshkov, A. V. Nalitov, and G. Malpuech, "Kibble-Zurek mechanism in topologically nontrivial zigzag chains of polariton micropillars," *Phys. Rev. Lett.* **116**, 046402 (2016).
12. P. St-Jean, V. Goblot, E. Galopin, A. Lemaître, T. Ozawa, L. Le Gratiet, I. Sagnes, J. Bloch, and A. Amo, "Lasing in topological edge states of a one-dimensional lattice," *Nat. Photonics* **11**, 651–656 (2017).
13. B. Bahari, A. Ndao, F. Vallini, A. El Amili, Y. Fainman, and B. Kanté, "Nonreciprocal lasing in topological cavities of arbitrary geometries," *Science* **358**, 636–640 (2017).
14. M. A. Bandres, S. Wittek, G. Harari, M. Parto, J. Ren, M. Segev, D. N. Christodoulides, and M. Khajavikhan, "Topological insulator laser: experiments," *Science* **359**, eaar4005 (2018).
15. P. R. Wallace, "The band theory of graphite," *Phys. Rev.* **71**, 622–634 (1947).
16. G. W. Semenoff, "Condensed-matter simulation of a three-dimensional anomaly," *Phys. Rev. Lett.* **53**, 2449–2452 (1984).
17. M. Katsnelson, K. Novoselov, and A. Geim, "Chiral tunnelling and the Klein paradox in graphene," *Nat. Phys.* **2**, 620–625 (2006).
18. L. Minhyun, S. Park, S. Hyunjae, S. Hyeonjin, K.-B. Kim, K. Yunhho, and S. Lee, "Lithium ion battery including nano-crystalline graphene electrode," U.S. patent App. 16/015,835 (28 March 2019).
19. L. Allen, M. W. Beijersbergen, R. J. C. Spreeuw, and J. P. Woerdman, "Orbital angular momentum of light and the transformation of Laguerre-Gaussian laser modes," *Phys. Rev. A* **45**, 8185–8189 (1992).
20. D. Rozas, C. T. Law, and G. A. Swartzlander, "Propagation dynamics of optical vortices," *J. Opt. Soc. Am. B* **14**, 3054–3065 (1997).
21. Z. Zhang, F. Li, G. Malpuech, Y. Zhang, O. Bleu, S. Koniakhin, C. Li, Y. Zhang, M. Xiao, and D. D. Solnyshkov, "Particlelike behavior of topological defects in linear wave packets in photonic graphene," *Phys. Rev. Lett.* **122**, 233905 (2019).
22. D. Song, D. Leykam, J. Su, X. Liu, L. Tang, S. Liu, J. Zhao, N. K. Efremidis, J. Xu, and Z. Chen, "Valley vortex states and degeneracy lifting via photonic higher-band excitation," *Phys. Rev. Lett.* **122**, 123903 (2019).
23. D. Song, V. Paltoglou, S. Liu, Y. Zhu, D. Gallardo, L. Tang, J. Xu, M. Ablowitz, N. K. Efremidis, and Z. Chen, "Unveiling pseudospin and angular momentum in photonic graphene," *Nat. Commun.* **6**, 6272 (2015).
24. Y. Plotnik, M. C. Rechtsman, D. Song, M. Heinrich, J. M. Zeuner, S. Nolte, Y. Lumer, N. Malkova, J. Xu, A. Szameit, Z. Chen, and M. Segev, "Observation of unconventional edge states in 'photonic graphene,'" *Nat. Mater.* **13**, 57–62 (2014).
25. M. Bellec, U. Kuhl, G. Montambaux, and F. Mortessagne, "Topological transition of Dirac points in a microwave experiment," *Phys. Rev. Lett.* **110**, 033902 (2013).
26. J. W. Fleischer, M. Segev, N. K. Efremidis, and D. N. Christodoulides, "Observation of two-dimensional discrete solitons in optically induced nonlinear photonic lattices," *Nature* **422**, 147–150 (2003).
27. T. Jacqmin, I. Carusotto, I. Sagnes, M. Abbarchi, D. D. Solnyshkov, G. Malpuech, E. Galopin, A. Lemaître, J. Bloch, and A. Amo, "Direct observation of Dirac cones and a flatband in a honeycomb lattice for polaritons," *Phys. Rev. Lett.* **112**, 116402 (2014).
28. M. Milićević, T. Ozawa, P. Andreakou, I. Carusotto, T. Jacqmin, E. Galopin, A. Lemaître, L. Le Gratiet, I. Sagnes, J. Bloch, and A. Amo, "Edge states in polariton honeycomb lattices," *2D Mater.* **2**, 034012 (2015).
29. M. Milićević, O. Bleu, D. D. Solnyshkov, I. Sagnes, A. Lemaître, L. L. Gratiet, A. Harouri, J. Bloch, G. Malpuech, and A. Amo, "Lasing in optically induced gap states in photonic graphene," *SciPost Phys.* **5**, 64 (2018).
30. A. V. Nalitov, G. Malpuech, H. Tercas, and D. D. Solnyshkov, "Spin-orbit coupling and the optical spin Hall effect in photonic graphene," *Phys. Rev. Lett.* **114**, 026803 (2015).
31. K. S. Novoselov, E. McCann, S. Morozov, V. I. Fal'ko, M. Katsnelson, U. Zeitler, D. Jiang, F. Schedin, and A. Geim, "Unconventional quantum Hall effect and Berry's phase of 2π in bilayer graphene," *Nat. Phys.* **2**, 177–180 (2006).
32. Y. Shen, *The Principles of Nonlinear Optics*, Wiley Classics Library (Wiley-Interscience, 2003).
33. W. Wagner, H. Haus, and J. Marburger, "Large-scale self-trapping of optical beams in the paraxial ray approximation," *Phys. Rev.* **175**, 256–266 (1968).
34. E. Brasselet, Y. Izdebskaya, V. Shvedov, A. S. Desyatnikov, W. Krolikowski, and Y. S. Kivshar, "Dynamics of optical spin-orbit coupling in uniaxial crystals," *Opt. Lett.* **34**, 1021–1023 (2009).
35. A. Ciattoni, G. Cincotti, and C. Palma, "Circularly polarized beams and vortex generation in uniaxial media," *J. Opt. Soc. Am. A* **20**, 163–171 (2003).
36. T. A. Fadeyeva and A. V. Vol'nyar, "Extreme spin-orbit coupling in crystal-traveling paraxial beams," *J. Opt. Soc. Am. A* **27**, 381–389 (2010).
37. K. Y. Bliokh, "Geometrodynamics of polarized light: Berry phase and spin Hall effect in a gradient-index medium," *J. Opt. A* **11**, 094009 (2009).
38. A. Aiello, N. Lindlein, C. Marquardt, and G. Leuchs, "Transverse angular momentum and geometric spin Hall effect of light," *Phys. Rev. Lett.* **103**, 100401 (2009).
39. S. M. Rytov, "On transition from wave to geometrical optics," *Dokl. Akad. Nauk SSSR* **18**, 263–267 (1938) [Markovski, B. and Vinitzky, S. I., eds., *Topological Phases in Quantum Theory* (World Scientific, 1989)].
40. J. Strohbehn and S. Clifford, "Polarization and angle-of-arrival fluctuations for a plane wave propagated through a turbulent medium," *IEEE Trans. Antennas Propag.* **15**, 416–421 (1967).
41. J. Zhang, S. Ding, H. Zhai, and A. Dang, "Theoretical and experimental studies of polarization fluctuations over atmospheric turbulent channels for wireless optical communication systems," *Opt. Express* **22**, 32482–32488 (2014).
42. V. V. Vladimirov, "On the rotation of the polarization plane along a curved ray," *Dokl. Akad. Nauk SSSR* **31**, 222–225 (1941).
43. M. V. Berry, "Quantal phase factors accompanying adiabatic changes," *Proc. R. Soc. London A* **392**, 45–57 (1984).
44. S. G. Lipson, "Berry's phase in optical interferometry: a simple derivation," *Opt. Lett.* **15**, 154–155 (1990).
45. L. D. Landau and E. M. Lifshitz, *Electrodynamics of Continuous Media* (Pergamon, 1984).
46. A. Pick and N. Moiseyev, "Polarization dependence of the propagation constant of leaky guided modes," *Phys. Rev. A* **97**, 043854 (2018).
47. A. Alberucci, C. P. Jisha, and S. Nolte, "Photonic potential for TM waves," *Opt. Lett.* **43**, 4949–4952 (2018).
48. C. P. Jisha and A. Alberucci, "Paraxial light beams in structured anisotropic media," *J. Opt. Soc. Am. A* **34**, 2019–2024 (2017).
49. K. Y. Bliokh, A. Niv, V. Kleiner, and E. Hasman, "Geometrodynamics of spinning light," *Nat. Photonics* **2**, 748–753 (2008).
50. T. Bardon-Brun, D. Delande, and N. Cherroret, "Spin Hall effect of light in a random medium," *Phys. Rev. Lett.* **123**, 043901 (2019).
51. D. Solnyshkov and G. Malpuech, "Chirality in photonic systems," *C. R. Phys.* **17**, 920–933 (2016).
52. J. Gea-Banacloche, Y.-Q. Li, S.-Z. Jin, and M. Xiao, "Electromagnetically induced transparency in ladder-type inhomogeneously broadened media: theory and experiment," *Phys. Rev. A* **51**, 576–584 (1995).
53. Z. Zhang, X. Liu, D. Zhang, J. Sheng, Y. Zhang, Y. Zhang, and M. Xiao, "Observation of electromagnetically induced Talbot effect in an atomic system," *Phys. Rev. A* **97**, 013603 (2018).
54. Z. Zhang, Y. Zhang, J. Sheng, L. Yang, M.-A. Miri, D. N. Christodoulides, B. He, Y. Zhang, and M. Xiao, "Observation of parity-time symmetry in optically induced atomic lattices," *Phys. Rev. Lett.* **117**, 123601 (2016).
55. Z. Zhang, L. Yang, J. Feng, J. Sheng, Y. Zhang, Y. Zhang, and M. Xiao, "Parity-time-symmetric optical lattice with alternating gain and loss atomic configurations," *Laser Photon. Rev.* **12**, 1800155 (2018).

56. Y. Zhu, S. Wang, and N. M. Mulchan, "Multilevel dark states in an inhomogeneously broadened open atomic system," *Phys. Rev. A* **59**, 4005–4011 (1999).
57. M.-C. Chang and Q. Niu, "Berry curvature, orbital moment, and effective quantum theory of electrons in electromagnetic fields," *J. Phys. Condens. Matter* **20**, 193202 (2008).
58. M. Matthews, B. P. Anderson, P. Haljan, D. Hall, M. Holland, J. Williams, C. Wieman, and E. Cornell, "Watching a superfluid untwist itself: recurrence of Rabi oscillations in a Bose-Einstein condensate," *Phys. Rev. Lett.* **83**, 3358–3361 (1999).
59. A. Leggett, *Quantum Liquids*, Oxford Graduate Texts (2006).
60. N. C. Zambon, P. St-Jean, M. Milićević, A. Lemaître, A. Harouri, L. Le Gratiet, O. Bleu, D. Solnyshkov, G. Malpuech, I. Sagnes, S. Ravets, A. Amo, and J. Bloch, "Optically controlling the emission chirality of microlasers," *Nat. Photonics* **13**, 283–288 (2019).